



Contemporary oceanic radiocarbon response to ocean circulation changes

Byju Pookkandy¹ · Heather Graven¹ · Adrian Martin²

Received: 14 October 2022 / Accepted: 23 February 2023 / Published online: 8 March 2023
© The Author(s) 2023

Abstract

Radiocarbon (^{14}C) is a valuable tracer of ocean circulation, owing to its natural decay over thousands of years and to its perturbation by nuclear weapons testing in the 1950s and 1960s. Previous studies have used ^{14}C to evaluate models or to investigate past climate change. However, the relationship between ocean ^{14}C and ocean circulation changes over the past few decades has not been explored. Here we use an Ocean-Sea-ice model (NEMO) forced with transient or fixed atmospheric reanalysis (JRA-55-do) and atmospheric ^{14}C and CO_2 boundary conditions to investigate the effect of ocean circulation trends and variability on ^{14}C . We find that $^{14}\text{C}/\text{C}$ ($\Delta^{14}\text{C}$) variability is generally anti-correlated with potential density variability. The areas where the largest variability occurs varies by depth: in upwelling regions at the surface, at the edges of the subtropical gyres at 300 m depth, and in Antarctic Intermediate Water and North Atlantic Deep Water at 1000 m depth. We find that trends in the Atlantic Meridional Overturning Circulation may influence trends in $\Delta^{14}\text{C}$ in the North Atlantic. In the high-variability regions the simulated variations are larger than typical ocean $\Delta^{14}\text{C}$ measurement uncertainty of 2–5‰ suggesting that $\Delta^{14}\text{C}$ data could provide a useful tracer of circulation changes.

Keywords Ocean modelling · Radiocarbon tracer · Circulation changes · AMOC · Decadal variability

1 Introduction

Accurate prediction of the future of the Earth's climate relies on our understanding of ocean circulation because of its role in governing air-sea exchange and storage of heat and carbon. Transient ocean tracers can provide unique information about ocean circulation as they are sensitive to various processes integrated over a range of timescales.

Radiocarbon (^{14}C) in dissolved inorganic carbon is a tracer with both natural and anthropogenic influences. ^{14}C is produced naturally in the atmosphere by the interaction of nitrogen atoms and cosmic rays and it decays with a 5700-year half-life. Fossil fuel emissions beginning from the Industrial Revolution reduce the ratio $^{14}\text{C}/\text{C}$ ($\Delta^{14}\text{C}$) in atmospheric CO_2 by adding CO_2 with no ^{14}C . Then, nuclear weapon testing in the 1950s and 1960s abruptly increased

^{14}C in the atmosphere (Rafter and Fergusson 1957; Nydal 1963).

Observations of bomb-produced ^{14}C in the ocean from the 1970s-1990s have provided strong constraints on the rate of air-sea gas exchange (Broecker et al. 1985; Sweeney et al. 2007). After entering the ocean via gas exchange, the $\Delta^{14}\text{C}$ distribution in the interior ocean is governed by advection–diffusion processes and radioactive decay. Radiocarbon has been used for many decades to understand ocean ventilation over a range of timescales corresponding to both natural and bomb radiocarbon, and to evaluate model representation of transport and water mass formation processes (Jain et al. 1995; England and Maier-Reimer 2001; Duffy et al. 1995; Guilderson et al. 2000; Gnanadesikan et al. 2004; Matsumoto and Key 2004; Grumet et al. 2005; Galbraith et al. 2011). Air-sea exchange was the dominant control on the rate of oceanic uptake of bomb-produced ^{14}C until the 1990s, but then the dominant control shifted to shallow-to-deep transport and mixing, which also regulate the uptake of anthropogenic CO_2 and are important for heat uptake (Graven et al. 2012; Khatiwala et al. 2013; Winton et al. 2013; DeVries et al. 2017).

✉ Byju Pookkandy
byjubhaskar@gmail.com

¹ Imperial College London, London, UK

² National Oceanography Center, Southampton, UK

Previous studies using radiocarbon to study recent ocean circulation have focused on the steady-state or average ocean circulation and have not examined variability in ocean circulation on decadal timescales. Tracer-based studies of recent ocean circulation variability have mainly relied on chlorofluorocarbons, which are entirely man-made and have been measured in the ocean since the 1970s. These studies have revealed variations in upper-ocean ventilation, which have impacts on ocean CO₂ uptake, although attributing the variability to internal or external drivers is challenging (Waugh et al. 2013; DeVries et al. 2017; Lester et al. 2020).

Radiocarbon may provide unique information about ocean circulation on decadal timescales, however, the relationships between recent ocean circulation and ¹⁴C variability has not yet been explored by global ocean models. In this study, we simulate $\Delta^{14}\text{C}$ in the ocean and examine how it is affected by circulation changes. We describe the implementation of radiocarbon tracer in the ocean model (Nucleus for European Modelling of the Ocean (NEMO)) and evaluate the performance of the model in simulating $\Delta^{14}\text{C}$ by comparing it to observations. We then analyze the differences in $\Delta^{14}\text{C}$ when the model is driven with fixed or time-varying atmospheric forcings and we suggest some potential mechanisms to explain the impact of variable forcing, although we do not perform a detailed analysis of the specific ocean circulation changes in the model. We use the simulations to explore the sensitivity of $\Delta^{14}\text{C}$ to ocean circulation changes, and to assess whether $\Delta^{14}\text{C}$ observations would likely be useful for data-driven detection of ocean circulation change.

2 Data and method

2.1 Ocean abiotic radiocarbon modelling

We used the global ocean circulation model Nucleus for European Modelling of the Ocean (NEMO) version 3.6 (Madec 2014), which is coupled to the Los Alamos sea-ice model (CICE, Rae et al. (2015)) with ~ 1 degree resolution. Vertically, the full depth water column is divided into 75 levels with thickness varying from 1 m (top 10 m depth) to ~ 200 m at depths below 3500 m. A detailed description of the model set-up and evaluation of its physical dynamics are given in Storkey et al. (2018), and briefly in Marzocchi et al. (2021). Therefore, here, we only provide a description of the new incorporation of ¹⁴C in the passive tracer module (Tracers in Ocean Paradigm, TOP) in NEMO.

Following the Ocean Model Intercomparison Project (Orr et al. 1999, 2017), radiocarbon is simulated using two prognostic tracers: dissolved inorganic carbon (DIC) and radiocarbon in DIC (DI¹⁴C). We use the “abiotic” formulation, which neglects any changes in dissolved inorganic carbon components due to biological activities and

ignores mass-dependent isotopic fractionation during air-sea exchange (Toggweiler et al. 1989). $\Delta^{14}\text{C}$ in the ocean is then calculated as $1000(\text{DI}^{14}\text{C}/\text{DIC} - 1)$, with units in ‰. This quantity can be directly compared to the observational data reported as $\Delta^{14}\text{C}$ since biological effects are presumed to be small (Joos et al. 1997).

Air-sea gas exchange is calculated with a quadratic wind speed parameterization of the piston velocity with a coefficient of $0.257 \text{ cm/h m}^2/\text{s}^2$ from Wanninkhof (2014), scaled by fractional ice cover. The alkalinity, for the estimation of the aqueous concentration of CO₂, is computed as a function of salinity, and the concentration of phosphate and silicate are set constant ($\text{SiO}_2 = 7.7e^{-3} \text{ mol/m}^3$ and $\text{PO}_4 = 5.1e^{-4} \text{ mol/m}^3$).

2.2 Simulations

2.2.1 Spinup simulation

We ran a long spin-up simulation to allow the model physics and ocean carbon cycle to reach a steady state, even in the deep ocean. The boundary conditions for atmospheric CO₂ and $\Delta^{14}\text{C}$ were prescribed to 1850 values of 284 ppm and ~ -4 ‰ respectively (Meinshausen et al. 2017; Graven et al. 2017). $\Delta^{14}\text{C}$ in the ocean was initialized at 0‰ and DIC was initialized from OMIP fields based on observations (<http://omip-bgc.lsce.ipsl.fr/>). The spin up was forced by repeating JRA-55-do neutral year (JRA-NY, Stewart et al. 2020) atmospheric data, which is a one year span (01-May-1990 to 30-April-1991) from JRA-55-do (version 1.3) data when major climate modes such as the North Atlantic Oscillation, Southern Oscillation and Southern Annular Mode were largely neutral. The model was integrated for 9000 years, when the drift in $\Delta^{14}\text{C}$ was less than 0.001 ‰/year over more than 99% of the oceanic volume, satisfying the OMIP criterion for steady-state (Orr et al. 2017). Temperature and salinity are also spun up after 9000 years so they do not have any trend or inter-annual variation. The DIC, DI¹⁴C, temperature and salinity fields at the end of the 9000 years spin-up were then used as initial conditions to perform historical simulations.

2.2.2 Historical simulations

We ran two simulations with historical atmospheric CO₂ and $\Delta^{14}\text{C}$ boundary conditions. The CO₂ concentrations for 1850 to 2014 are from (Meinshausen et al. 2017) and the data over 2015 to 2020 are from NOAA’s Global Monitoring Laboratory <https://gml.noaa.gov/ccgg/trends/global.html>. Atmospheric $\Delta^{14}\text{C}$ is from Graven et al. (2017) for the period 1850 to 2015 and from the simulated transient $\Delta^{14}\text{C}$ for SSP2-4.5 over 2016–2020 (Graven et al. 2020). Global mean values are used for the CO₂ boundary

condition while three zonal bands (90° S– 30° S, 30° S– 30° N, 30° N– 90° N) are used for $\Delta^{14}\text{C}$. One simulation ("Hist") was forced with inter-annually varying JRA-55-do atmospheric reanalysis data (version 1.5, Tsujino et al. (2018)), which is available for the period 1958 through 2020 at 3-hour intervals. The JRA-55-do data is cycled over 1850 to 2020, where the 1850 atmospheric forcing corresponds to the year 1975. The other simulation ("Hist-NYF") was forced with the JRA-NY atmospheric data ('NY' stands for Neutral Year and 'NYF' means Neutral Year Forced) in every year. This includes seasonal variation in the forcing data but no inter-annual variability.

Then, we ran two simulations with fixed atmospheric CO_2 and $\Delta^{14}\text{C}$ boundary conditions, using 1850 values. Again, one simulation ("Fix") was forced with inter-annually varying JRA-55-do atmospheric reanalysis data and the other ("Fix-NYF") was forced with JRA-NY atmospheric data.

The "Hist" simulation represents the real world ocean while the "Fix-NYF" simulation is a control simulation continuing the spin-up simulation, and the "Hist-NYF" and "Fix" simulations allow us to examine the effect of changing circulation on total $\Delta^{14}\text{C}$ and on natural $\Delta^{14}\text{C}$.

Table 1 Date of $\Delta^{14}\text{C}$ repeat sections available in GLODAP and used for decadal comparisons

Transects	1990s Year–Months	2000s	2010s
A16	1991–03, 08, 09 1992–10, 11	2005–01, 02 2006–02, 03	2014–03, 04 2015–04, 05, 06
P16	1988–11 1989–04 1993–07, 08	2005–01, 02	2013–08, 10, 12 2014–02

2.3 Ocean observations

We use hydrographic survey data for $\Delta^{14}\text{C}$ from the Global Ocean Data Analysis Project (GLODAP v2.2020) data inventory (Key et al 2004; Olsen et al. 2020) to evaluate the model. We focus on two meridional sections, one in the Atlantic along roughly 30° W (A16) and the other in the Pacific Ocean along roughly 150° W (P16). We compare the simulated and observed changes in $\Delta^{14}\text{C}$ over three decades (year and months of sampling can be found in Table 1). We bin the observations by 2° in latitude and discrete vertical depths over the years the 1990s, 2000s and 2010s available in Table 1 and linearly interpolated $\Delta^{14}\text{C}$ for bins with no data. In the results, figures related to observational data show colour for each bin and have a blocky appearance, whereas figures related to only model output show smooth contours.

3 Results

3.1 Simulated bomb ^{14}C inventory and air-sea fluxes

First, we evaluate the globally-integrated oceanic inventories of bomb ^{14}C , defined as the excess radiocarbon relative to the year 1950 (Broecker et al. 1985), in the NEMO model. The simulated inventories are consistent with the observation-based estimates of Naegler (2009) for the GEOSECS data from the 1970s and the WOCE data from the 1990s (Fig. 1a). The inventory stops increasing around 2012 and starts to decrease. The time at which the ^{14}C inventory peaks depends on the efficiency of mixing processes and varies between models (Graven et al. 2012). For example, the CCSM model inventory showed an earlier peak around

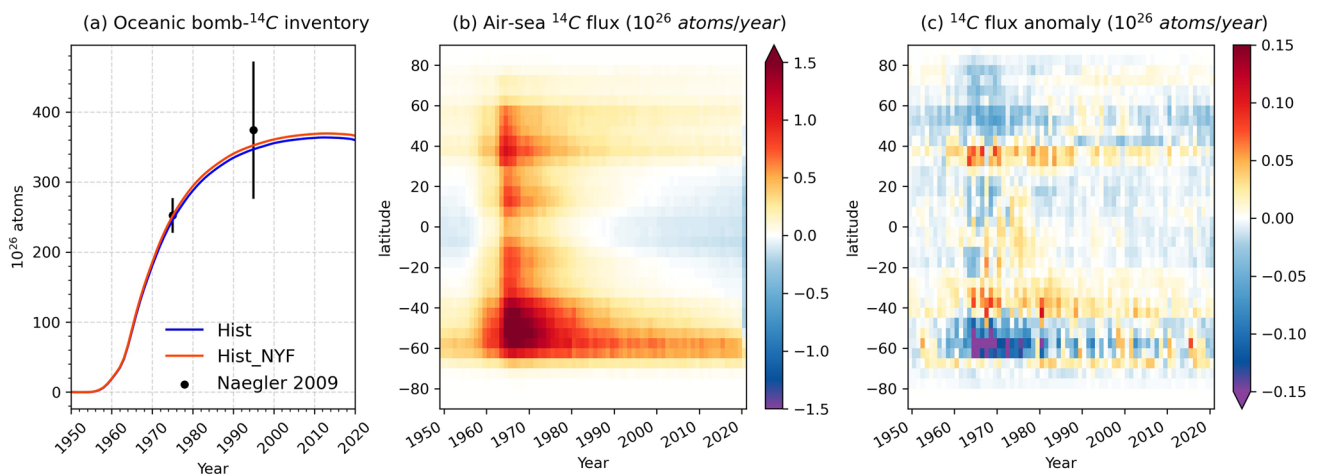


Fig. 1 (a) Globally integrated oceanic radiocarbon inventory relative to the year 1950, (b) zonally integrated air-to-sea radiocarbon flux in 5 degree latitude bins for the Hist simulation, and (c) radiocarbon flux anomaly between Hist and Hist-NYF simulations

2000, while the ECCO model inventory peaks a bit later in 2015–17 (Khatiwala et al. 2018). Comparing the Hist and Hist-NYF simulations, the Hist-NYF inventory is slightly higher for the period 1980–2020.

Patterns of net flux of ^{14}C into the ocean are similar to other models (Fig. 1b; Graven et al. 2012). There is a dramatic increase in ^{14}C flux after the bomb testing in the 1950s and 1960s, with the largest fluxes in the Southern Ocean. The net air-sea flux changed its sign to negative in the low latitudes by the mid-1990s in response to ocean ^{14}C uptake and decreasing atmospheric $\Delta^{14}\text{C}$ that caused the ocean to have higher $\Delta^{14}\text{C}$ than the atmosphere. The area of ^{14}C outgassing extends progressively poleward with time. However, the Southern Ocean remains a strong sink for ^{14}C .

Comparing the Hist and Hist-NYF simulations (Fig. 1c) shows that the largest effect of the inter-annual forcing is to decrease the influx of ^{14}C to the Southern Ocean in the 1960s–70s. The effect of the inter-annual forcing is positive south of 65°S and between 25 and 45° latitudes in both hemispheres, and negative north of 45°N . To a large extent the positive or negative differences are sustained through

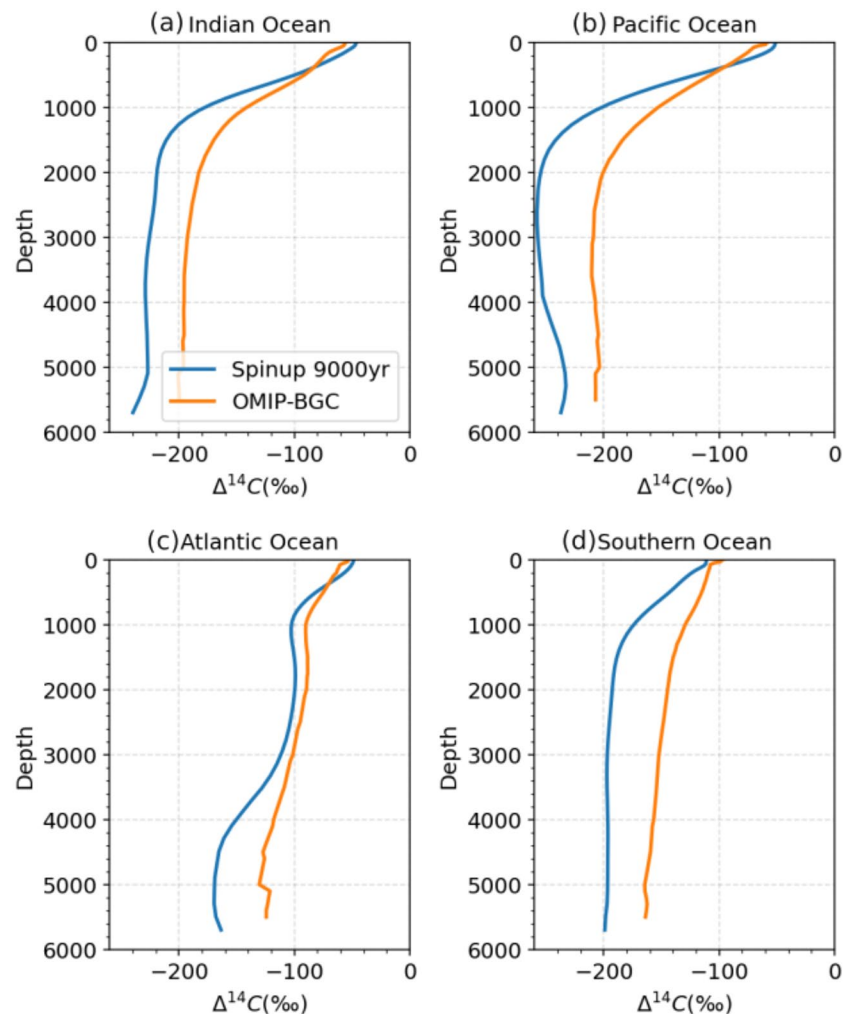
the whole period, however, in the tropics and the Southern Ocean the fluxes switch between higher and lower fluxes with the inter-annual vs neutral year forcing. Sustained differences could suggest the JRA-NY forcing is significantly different from the average forcing over the JRA period 1958–2020 in those regions.

3.2 Modeled $\Delta^{14}\text{C}$ vs observations

$\Delta^{14}\text{C}$ at the end of the long spin-up is $\sim 40\%$ lower than the estimate of natural radiocarbon in GLODAP (Key et al. 2004) at depths below the thermocline in most regions (Fig. 2). Part of the discrepancy can be attributed to a bias in the estimate of natural radiocarbon below the thermocline in GLODAP (Sweeney et al. 2007; DeVries and Holzer 2019). However, $\Delta^{14}\text{C}$ in NEMO is still too low, indicating that the ventilation of the deep ocean in NEMO is too sluggish.

Figures 3 and 4 show the vertical $\Delta^{14}\text{C}$ profiles for the Hist simulation and the observations along the two meridional sections in the Atlantic and Pacific Oceans. Here, the model data is re-sampled to match the location and time of

Fig. 2 Basin-wide mean profiles of $\Delta^{14}\text{C}$ from our 9000 year spinup simulation and the data provided by OMIP-BGC, based on GLODAP



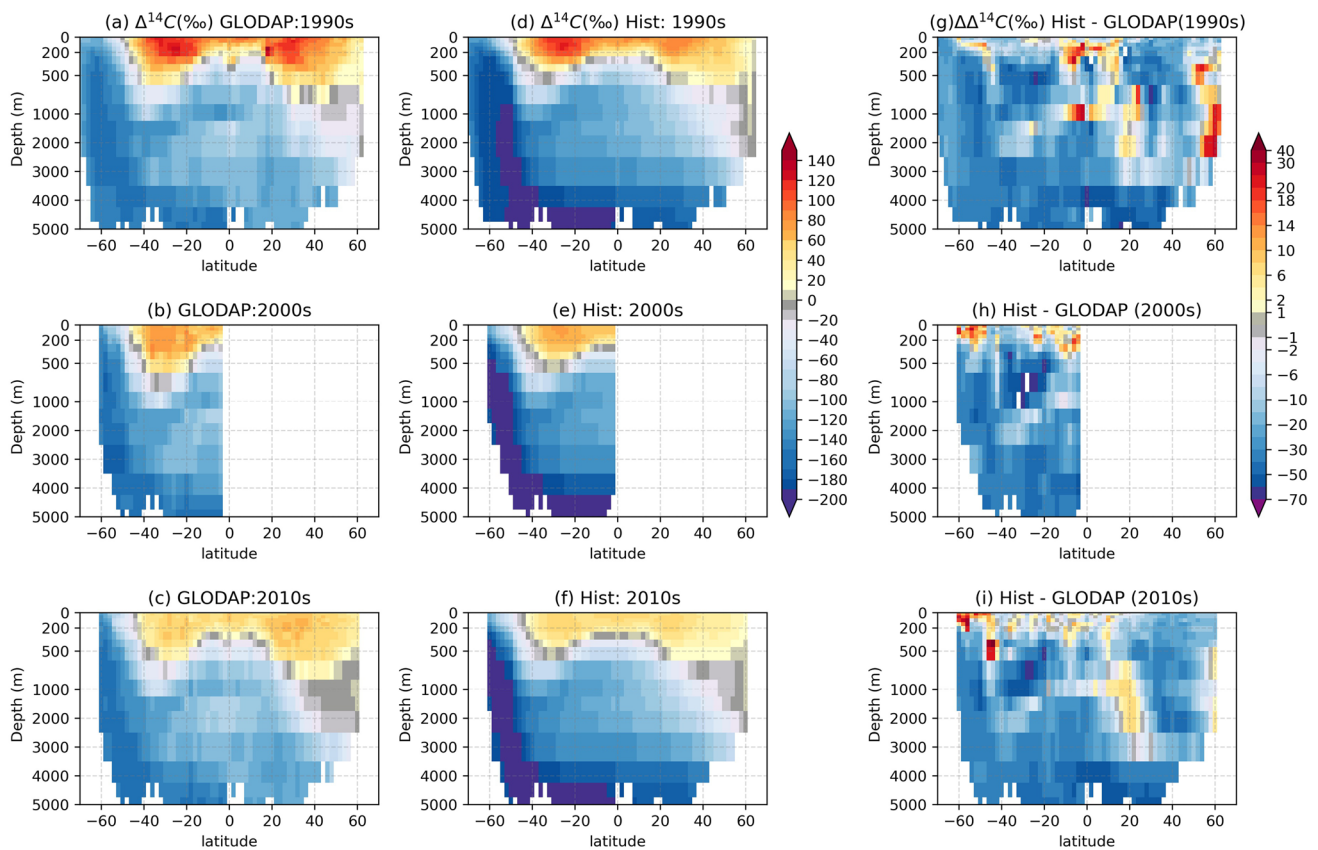


Fig. 3 Observed (a–c) and simulated (d–f) $\Delta^{14}\text{C}$ along the A16 section in the Atlantic Ocean in the three time periods (rows). No observations are available for the North Atlantic in the 2000s. (g–i) represents the bias, modeled—observed $\Delta^{14}\text{C}$. The units for all panels are ‰

the observations (see Table 1) and binned in the same way as the observations (Sect. 2.3).

The observed $\Delta^{14}\text{C}$ profiles in the Atlantic Ocean (Fig. 3a–c) show high $\Delta^{14}\text{C}$ in the subtropical gyres down to 500m and in the shallow tropical ocean. In the North Atlantic, high $\Delta^{14}\text{C}$ penetrates deeply, below 2000m, due to deep water formation while in the Southern Ocean $\Delta^{14}\text{C}$ is low in the deep ocean up to the surface due to upwelling and limited air-sea equilibration. The profile is similar in the Pacific, but without the deep water formation and high $\Delta^{14}\text{C}$ in the north (Fig. 4a–c). A decrease in $\Delta^{14}\text{C}$ from the 1990s to 2010s is observed above 500m in both the Atlantic and the Pacific following the decrease in atmospheric $\Delta^{14}\text{C}$.

These features are qualitatively well captured in the model simulation (middle column d–f in Fig. 3 and 4) but there are biases in the model. The model biases are largely negative ($> -50\%$), especially in deep waters and in the Southern Ocean (right column e–f in Figs. 3 and 4). This negative bias in recent decades is similar to the bias in natural radiocarbon in the spin-up simulation (Fig. 2). Patches of positive bias are present, primarily in the tropics and high latitudes. The largest positive bias ($> 40\%$) is found in the north Pacific at depths shallower than 500m. With negative

biases at depth and positive biases in the shallow ocean, NEMO overestimates the vertical gradients in $\Delta^{14}\text{C}$ in these regions.

We also compare the changes in $\Delta^{14}\text{C}$ ($\Delta\Delta^{14}\text{C}$) over decades in the simulations with the observations. Figure 5 shows the normalized change in $\Delta^{14}\text{C}$ from the 1990s to the 2010s in observations and in the Hist simulation along A16 and P16. $\Delta\Delta^{14}\text{C}$ is negative in shallow water (surface to ~ 300 m) and positive in the thermocline depths. The negative values in the surface layer arise from downward transport and from outgassing of ^{14}C while the positive values in the thermocline indicate ^{14}C has been transported from the surface layers and accumulated (Graven et al. 2012). This pattern is well-captured in the model. However, the rate of change is underestimated. In the model, the decreases in shallow layers are too weak and the increases at depth are also too weak, by $\sim 5\%$ per decade for the strongest changes. Underestimates of $\Delta\Delta^{14}\text{C}$ may indicate that the model is too efficient at dispersing ^{14}C , similar to the ECCO model (Graven et al. 2012). In contrast, the CCSM model overestimated the magnitude of changes for the 1990s to 2000s in Graven et al. (2012), indicating that CCSM did not transfer enough bomb ^{14}C into deep layers, which may have

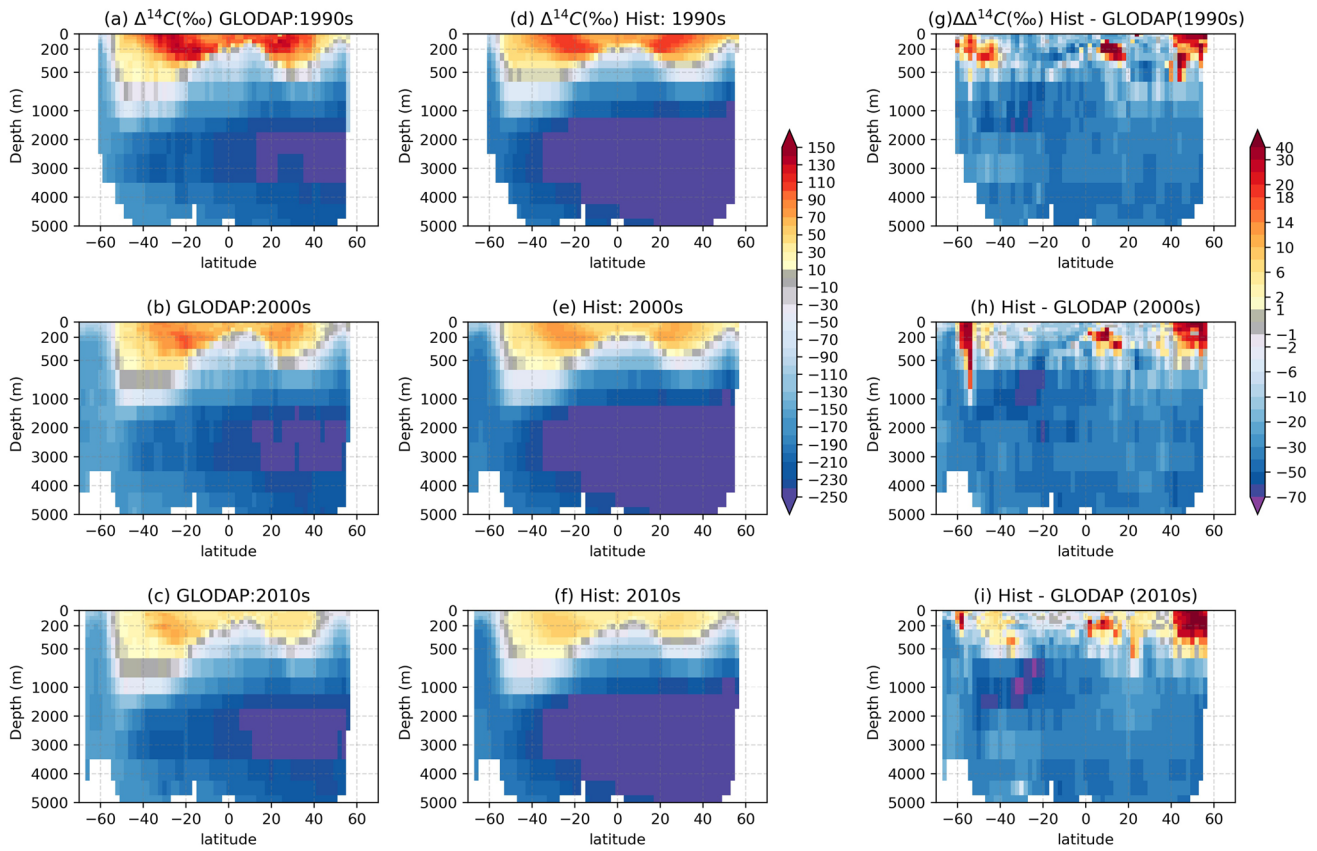


Fig. 4 Same as in Fig. 3 but along the P16 section in the Pacific Ocean

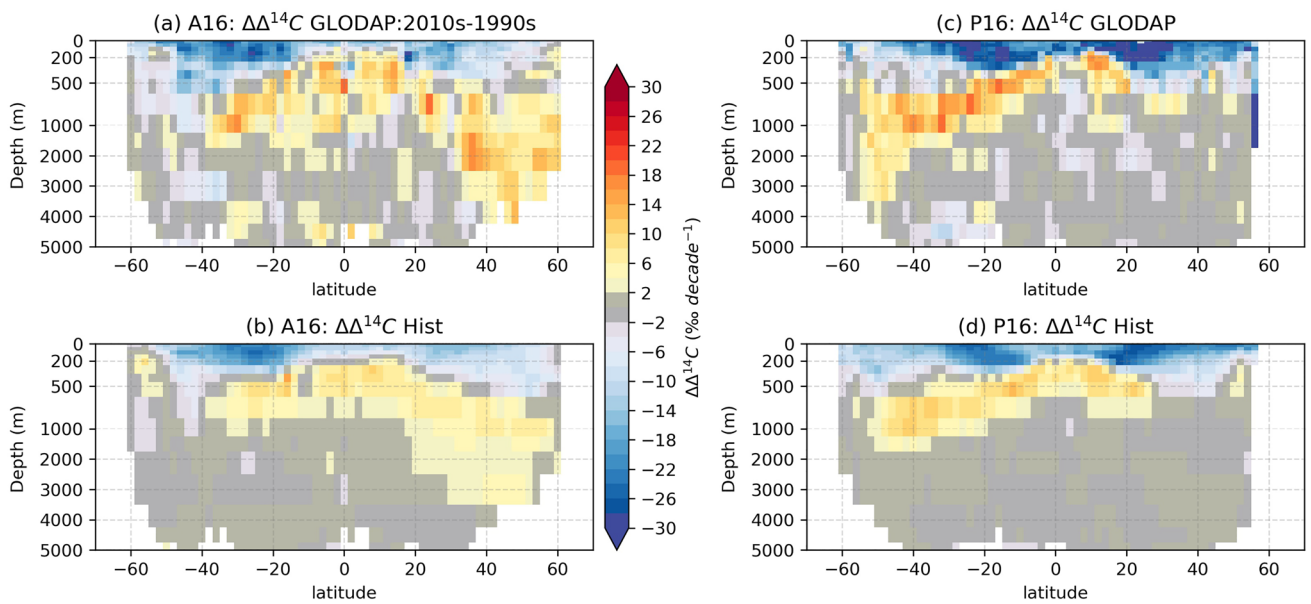


Fig. 5 Changes in $\Delta^{14}\text{C}$ between 1990s and 2010s along A16 (**a, b**) and P16 (**c, d**). Observations are shown in the top row and the Hist simulations in the bottom row. Note that the values are normalised to

‰ per decade and the Hist values are re-sampled to match the exact location and time in GLODAP observations

resulted in part from errors in modeled density. Interestingly, this result seems to contrast with the comparison for natural radiocarbon (Fig. 2), which indicated NEMO was transporting ^{14}C to the deep ocean too slowly, suggesting there may be different biases for decadal-scale vs millennial-scale transport in the model.

3.3 Effect of variable forcing on $\Delta^{14}\text{C}$ changes along the sections

In this section, we discuss how the radiocarbon distribution is impacted by the change in ocean circulation or gas exchange arising from variable atmospheric forcing. Here we show the distribution along the transects in the model grid itself rather than re-gridding to match observations. We show the average over the years sampled on each section when sections were observed over multiple years (Table 1). To show the effect of variable forcing on total $\Delta^{14}\text{C}$ changes, we plot the difference: $\Delta\Delta^{14}\text{C}$ simulated in Hist minus $\Delta\Delta^{14}\text{C}$ simulated in Hist-NYF ($\Delta\Delta\Delta^{14}\text{C}$). So, the difference between Hist and Hist NYF ignores the effect of temporal changes in atmospheric $\Delta^{14}\text{C}$ and describes how the distribution of $\Delta^{14}\text{C}$ changes in the inter-annually varying ocean compared to the steady-state ocean. We also consider the effect on natural radiocarbon by plotting $\Delta\Delta^{14}\text{C}$ simulated in Fix minus $\Delta\Delta^{14}\text{C}$ simulated in Fix-NYF, which is included in the main text. In the supplement, we additionally plot the effect on bomb radiocarbon. We note that the differences in $\Delta\Delta^{14}\text{C}$ between approximately decadal hydrographic cruises can reflect variations in forcing and circulation over a range of timescales: inter-annual, decadal and multi-decadal.

In the Pacific, along the P16 transect, the decadal changes in atmospheric forcing caused significant variability in $\Delta^{14}\text{C}$

distribution in the upper 1000 m water depths (Fig. 6). Potential density also exhibits significant variability (Fig. 6e, f) in the upper 1000 m water depths associated with the changes in atmospheric forcings. Moreover, the differences in $\Delta\Delta^{14}\text{C}$ are largely anti-correlated with changes in potential density (Fig. 6e, f). Since $\Delta^{14}\text{C}$ typically decreases with depth and potential density increases with depth, much of the variation may arise from displacement of isopycnal surfaces.

$\Delta\Delta\Delta^{14}\text{C}$, the difference in the $\Delta^{14}\text{C}$ change from one decade to the next in the JRA-interannually-forced simulation minus the JRA-NY-forced simulation, exhibits a dipole pattern in the Northern Hemisphere. From the 1990s to 2000s, $\Delta\Delta^{14}\text{C}$ with variable forcing is 15‰ decade⁻¹ higher around 20° N at 200–1000 m depths, while around 40° N it is >10‰ decade⁻¹ lower (Fig. 6c). From the 2000s to 2010s, the sign has flipped, at 20° N $\Delta\Delta^{14}\text{C}$ is >10‰ decade⁻¹ lower and at 40° N >5‰ decade⁻¹ higher (Fig. 6d). Potential density fields also exhibit similar feature (Fig. 6e, f). This indicates a change of circulation pattern between the two decades as it represents the change in $\Delta\Delta^{14}\text{C}$ between dynamic and steady-state simulations and it is reflected in potential density. Change in subtropical gyre subduction related to changes in atmospheric forcings (Schneider et al. 1999; Qu and Chen 2009) could be causing the $\Delta\Delta^{14}\text{C}$ and potential density changes. In the Southern Hemisphere, $\Delta\Delta\Delta^{14}\text{C}$ is small for the 1990s–2000s. For the 2000s–2010s, $\Delta\Delta\Delta^{14}\text{C}$ is stronger and there is a pattern of lower $\Delta\Delta^{14}\text{C}$ south of 50° S and higher $\Delta\Delta^{14}\text{C}$ north of 50° S. This pattern could reflect faster ventilation of Subantarctic Mode Water and faster upwelling of Circumpolar Deep Water, as found by Waugh et al. (2013) using CFCs but in the previous period (1990s–2000s). Both natural (Fig. 6a, b) and total radiocarbon (Fig. 6c, d) show similar patterns in response to changes

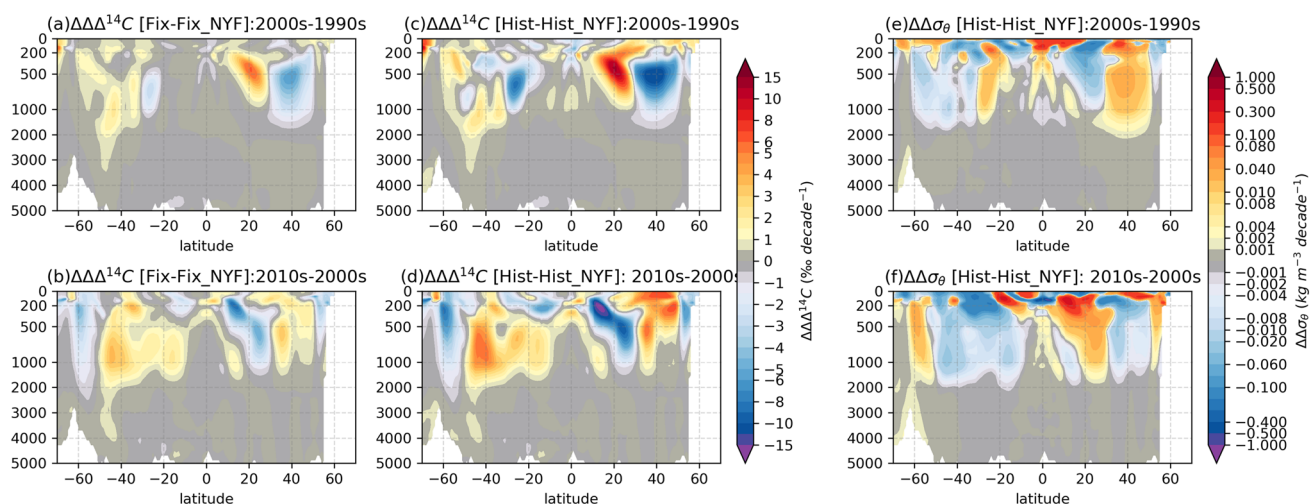


Fig. 6 The effect of variable forcing on changes in $\Delta^{14}\text{C}$ over decades along P16 in the Pacific Ocean. Difference in $\Delta\Delta^{14}\text{C}$ between Fix and Fix-NYF, representing the normalised changes in natural $\Delta^{14}\text{C}$ (a,

b). Difference in $\Delta\Delta^{14}\text{C}$ between Hist and Hist-NYF, representing the normalised changes in total $\Delta^{14}\text{C}$ (c, d). The changes in potential density in the Hist and Hist-NYF simulation (e, f)

in atmospheric forcing, showing that natural (Fig. 6a, b) and bomb $\Delta^{14}\text{C}$ (Supplementary SFig. 1) are affected in similar ways.

The difference in the decadal rate of change of $\Delta^{14}\text{C}$ due to circulation changes along the A16 transect in the Atlantic (Fig. 7a–d) is different from the Pacific transect. In the Atlantic, changes occur over the entire water column, while in the Pacific significant changes are visible only in the upper 2000m water depths. This is because strong transport in the North Atlantic even in the deep ocean occurs on decadal timescale, while Pacific deep ocean circulation happens on longer timescales. The simulation with the variable atmospheric forcing shows higher $\Delta\Delta^{14}\text{C}$ in the North Atlantic north of 40°N , 500–2000m depth, with smaller and more variable differences in other regions. Again, the patterns are similar for natural $\Delta^{14}\text{C}$ (Fig. 7a, b) and for total $\Delta^{14}\text{C}$ (Fig. 7c, d), but the primary driver of the signal is bomb ^{14}C .

For the region north of 40°N , 500–2000m, shown in the box in Fig. 7, higher $\Delta^{14}\text{C}$ is accompanied by both decreases (1990s–2000s) and increases (2000s–2010s) in potential density (Fig. 7e, f). Elsewhere, $\Delta\Delta^{14}\text{C}$ and potential density changes are anti-correlated, as in the Pacific transect. We will explore the North Atlantic region in the box in Fig. 7 in more detail in the next section.

3.4 North Atlantic $\Delta^{14}\text{C}$

Figure 8a shows the time series of the difference between $\Delta^{14}\text{C}$ in the Hist simulation and $\Delta^{14}\text{C}$ in the Hist-NYF simulation, averaged in the box shown in Fig. 7 (50°N – 60°N , 500–1000 m). $\Delta\Delta^{14}\text{C}$ (the difference between Hist and Hist-NYF) exhibits a decreasing tendency from

1958 to 1988 with decadal-scale oscillations that peak during 1972–74 and then during 1983–85. After 1988, $\Delta\Delta^{14}\text{C}$ shows a monotonic increase without oscillations. It reached $\sim -15\%$ in 1988 and increased to greater than zero after 2000.

The pattern of $\Delta^{14}\text{C}$ change is shown in more detail for the vertical column down to 3000m (50°N – 60°N) in Fig. 9. In the 1970s, high $\Delta^{14}\text{C}$ is much more concentrated at the surface in Hist than in Hist-NYF. After 2000, $\Delta^{14}\text{C}$ is higher in Hist than in Hist-NYF down to about 2000 m.

The $\Delta\Delta^{14}\text{C}$ peaks in 1972–74 and 1983–85 align with deep winter mixed layers that transported more bomb ^{14}C into deeper layers (Figs. 8c, 9). The lack of such events after 1988 may result from the weaker vertical gradient in $\Delta^{14}\text{C}$ (Fig. 9), and/or from less variability in the mixed layer depth (Fig. 8c). The mixed layer depth in Hist-NYF in this region is actually much deeper than the average in Hist (Fig. 8c) which appears to have accentuated the ^{14}C transport into the interior North Atlantic during the period 1960–90 for Hist-NYF as compared to Hist.

The longer-term pattern of decreasing $\Delta\Delta^{14}\text{C}$ until 1988 and then increasing $\Delta\Delta^{14}\text{C}$ appears to be more in phase with AMOC than with the mixed layer depth, potential density, or net heat flux (Fig. 8). There is a good correlation between $\Delta\Delta^{14}\text{C}$ and the difference in AMOC over 1958–2020 ($r = -0.53$). A stronger AMOC could ventilate $\Delta^{14}\text{C}$ quickly to and away from the location, possibly reducing the amount of radiocarbon there, whereas a weaker AMOC could result in higher $\Delta^{14}\text{C}$ because of slow ventilation. In contrast, the longer term trend of mixed layer depth is to increase while $\Delta\Delta^{14}\text{C}$ is decreasing, which is the opposite relationship as found for the individual years with high mixed layers that also had high $\Delta\Delta^{14}\text{C}$.

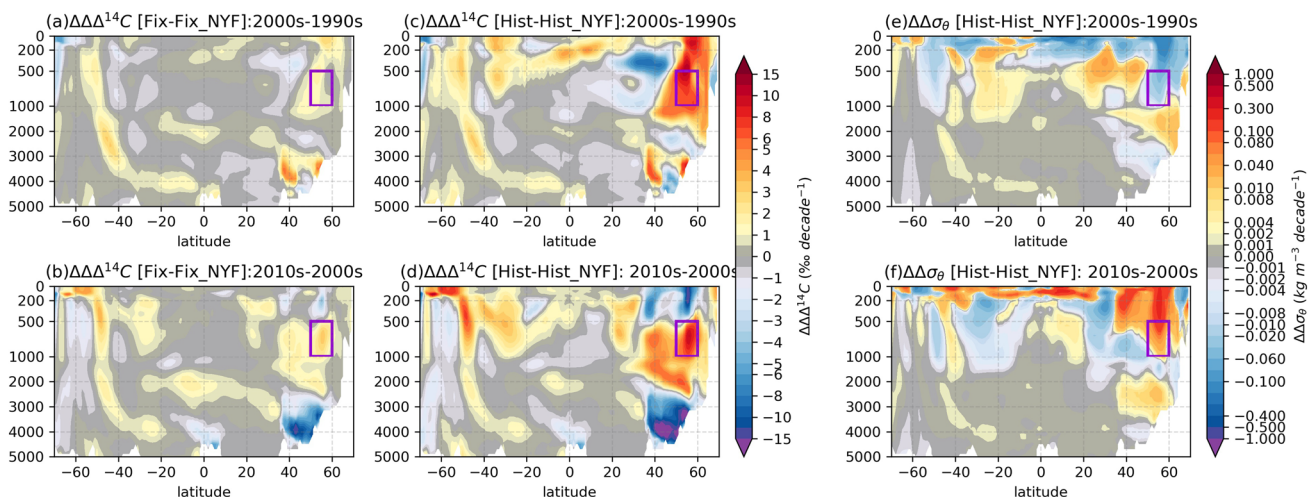
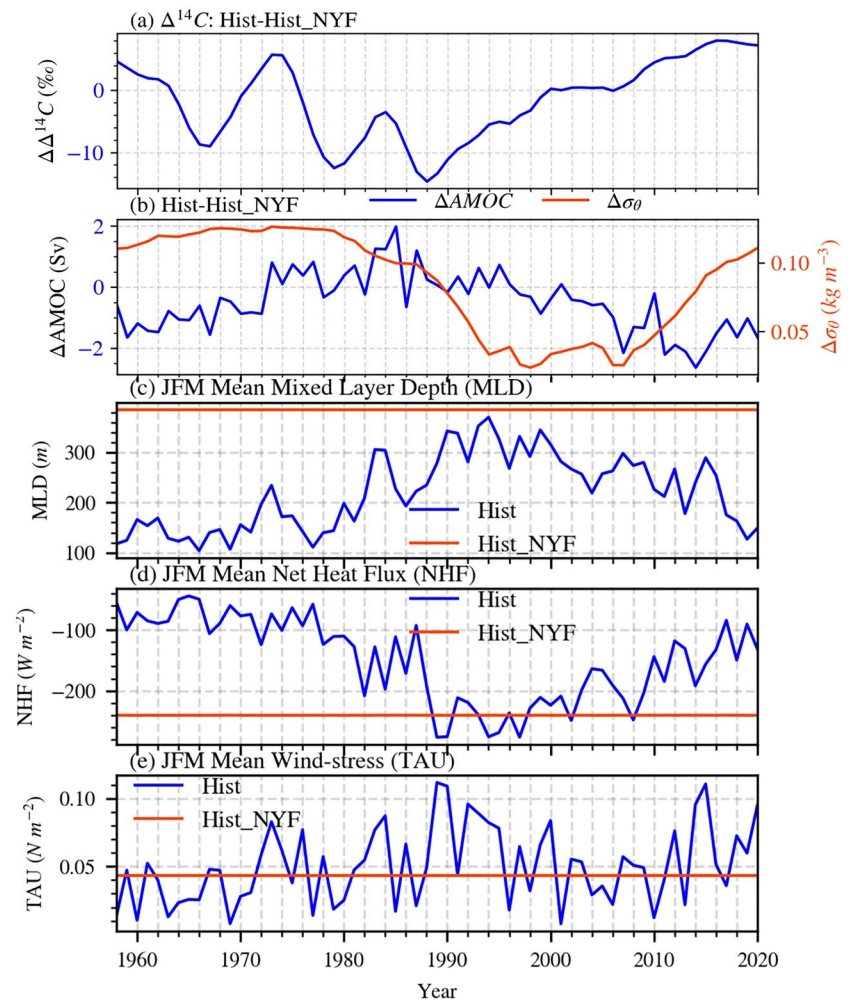


Fig. 7 Same as in Fig. 6 but along A16 in the Atlantic Ocean. The box in the figure points to the correlation ambiguity between $\Delta\Delta^{14}\text{C}$ and $\Delta\Delta\sigma$

Fig. 8 Time series of simulated variables in the North Atlantic, averaged over latitude 50–60° N, longitude 20–40° W, depth 500–1000m (a) anomaly in $\Delta^{14}\text{C}$ and (b) anomaly in potential density (σ) and AMOC (latitude–depth mean); latitude–longitude box averaged (c) winter mean (January–February–March–JFM) mixed layer depth (MLD) (d) winter mean net heat flux (NHF) and e winter mean wind-stress (TAU)



Thus, our hypothesis is that the variability in MLD acts to determine the $\Delta^{14}\text{C}$ distribution at local and annual scales (when the vertical gradients are large) while AMOC variability impacts the $\Delta^{14}\text{C}$ distribution on a multi-decadal timescale. The variability in winter MLD is largely modulated by net heat flux (NHF, Fig. 8d) and the wind-stress (TAU, Fig. 8E; Alexander et al. 2000; Pookkandy et al. 2016). Therefore, the short time-scale variability in rate of accumulation of $\Delta^{14}\text{C}$ in the interior ocean is influenced by the atmospheric conditions at the time of air-sea exchange (Marzocchi et al. 2021).

3.5 Global map of difference in radiocarbon distribution due to circulation changes

Changes in ocean circulation resulting from varying atmospheric forcing cause changes in the $\Delta^{14}\text{C}$ distribution in the surface and interior ocean. Figure 10a–d shows the mean difference in $\Delta^{14}\text{C}$ between Hist and Hist-NYF 1991 to 2020 at the surface, 300m, 1000m, and 3000m depths. Figure 10e–h

shows the standard deviation of the difference over 1991 to 2020.

The areas of the surface ocean with the largest differences and the largest standard deviations of the differences between Hist and Hist-NYF are upwelling areas such as the eastern Pacific, the subpolar gyres in the North Pacific and North Atlantic, and the Southern Ocean (Fig. 10). These areas are where vertical exchanges of deeper ^{14}C -depleted waters can vary and affect the surface $\Delta^{14}\text{C}$ values. On average, surface ^{14}C was higher in the Northeast Atlantic, Southeast Pacific and north of the Ross Sea, and lower in the North Pacific and north of the Weddell Sea over 1991–2020 in Hist as compared to Hist-NYF. The differences are up to $\pm 12\%$. Differences at 300m are largely similar in pattern to differences at the surface, but with stronger magnitudes of up to $\pm 20\%$ or more.

In the North Pacific shallow subpolar waters ($<300\text{m}$), $\Delta^{14}\text{C}$ in the Hist simulation is 20% lower than Hist-NYF (Fig. 10). Over 1991–2020, these shallow ocean regions are decreasing in $\Delta^{14}\text{C}$, so the negative value indicates a stronger decrease in Hist due to differences in circulation

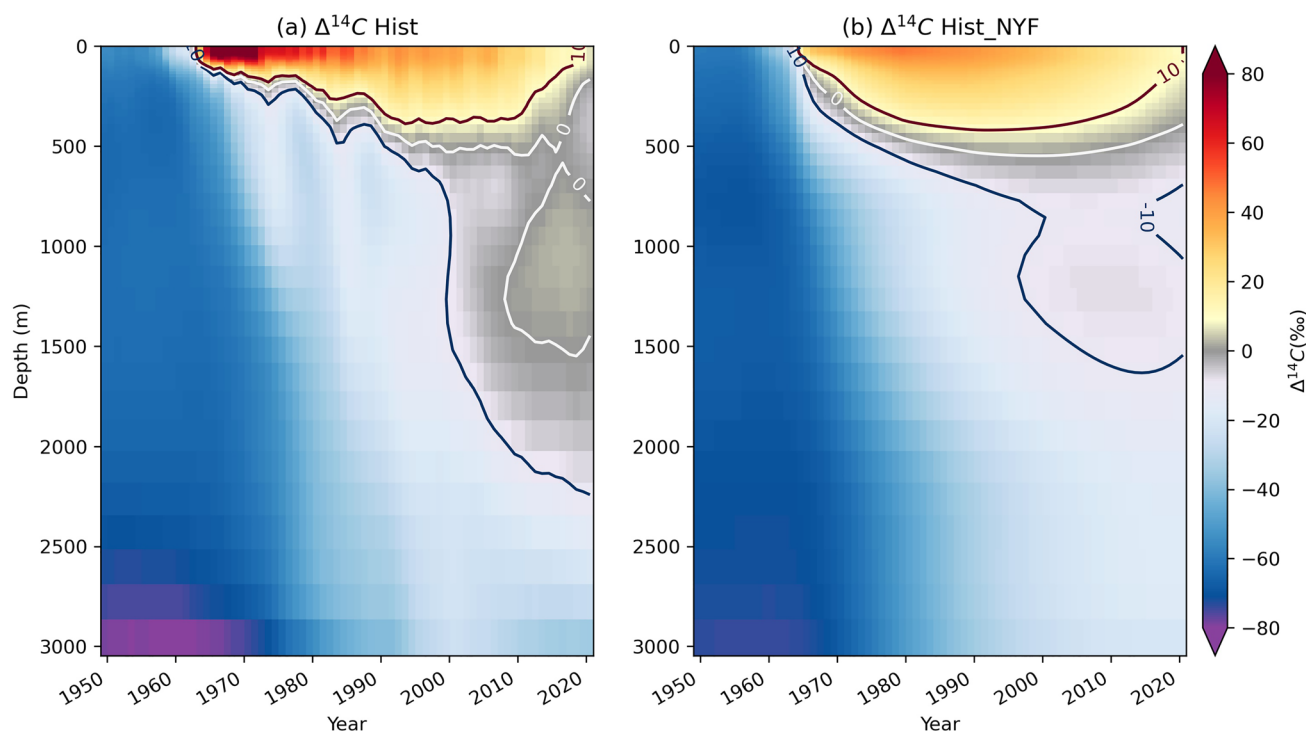


Fig. 9 Plot of $\Delta^{14}\text{C}$ vs time and depth averaged in the box $50\text{--}60^\circ\text{N}$ and $20\text{--}40^\circ\text{W}$ (north Atlantic) for the (a) Hist simulation and (b) Hist-NYF

from Hist-NYF that could be related to stratification, gyre dynamics and/or upwelling.

At $\sim 1000\text{m}$ depth, the largest differences between Hist and Hist-NYF and variability in Hist are found in the Southwest Pacific and Southern Indian Oceans, with the mean difference showing a dipole structure in the North Atlantic that is opposite to the pattern at 300m (Fig. 10). The subduction of radiocarbon rich water in the Southern Ocean as mode and intermediate water (SAMW and AAIW) or so called thermocline ventilation are the primary cause of high anthropogenic carbon sequestration in the Southern hemisphere midlatitude intermediate depths (Downes et al. 2009, 2017; Sallee et al. 2010, 2012; Jenkins et al. 2010). Moreover, Marzocchi et al. (2021) have presented evidence (using dye tracer experiments) that dye tracer in these locations is associated with a timescale of more than 20–25 years leading to accumulation over time. Hence, observing variation in radiocarbon in these regions could help to identify and understand ventilation changes in Southern Mode and Intermediate waters (Fig. 6; Waugh et al. 2013).

Radiocarbon variability is small at 3000m depths except for the deep western boundary current of the Atlantic, which shows lower $\Delta^{14}\text{C}$ in Hist than Hist-NYF. This is consistent with our hypothesis of the effect of slower AMOC-related ventilation on ^{14}C in Hist over 1990–2020 or previous decades, leading to more ^{14}C at mid-depths of $500\text{--}1000\text{m}$ in the North Atlantic but less ^{14}C further along the ventilation

route in the deep western boundary current. Deeper mixed layers in the North Atlantic in Hist-NYF than in Hist may also have driven stronger transport of ^{14}C into North Atlantic Deep Water.

3.6 Discussion and summary

The NEMO model simulations explored here show how $\Delta^{14}\text{C}$ in the ocean responds to changes in atmospheric forcing. The simulations are integrated from 1850 to 2020 using JRA-55-do inter-annually varying and neutral-year atmospheric reanalysis data, where the initial boundary fields of ocean DIC, DI^{14}C , dynamic and thermodynamic fields are from a 9000-year spin-up simulation. The model captures the large-scale $\Delta^{14}\text{C}$ pattern and its change over time along the cruise tracks in the Pacific (P16) and Atlantic (A16) oceans. However, the model is biased low by more than 20‰ in the interior ocean and the magnitude of changes between the 1990s and 2010s is underestimated. The biases are somewhat different to the findings for ECCO and CCSM, where weak temporal changes were associated with high biases in deep ocean $\Delta^{14}\text{C}$ (Graven et al. 2012), perhaps indicating that biases in ocean circulation can be different for different timescales.

Analyzing the $\Delta^{14}\text{C}$ changes over decades for the variable and fixed circulation shows a strong large-scale association with changes in potential density, indicative of vertical or

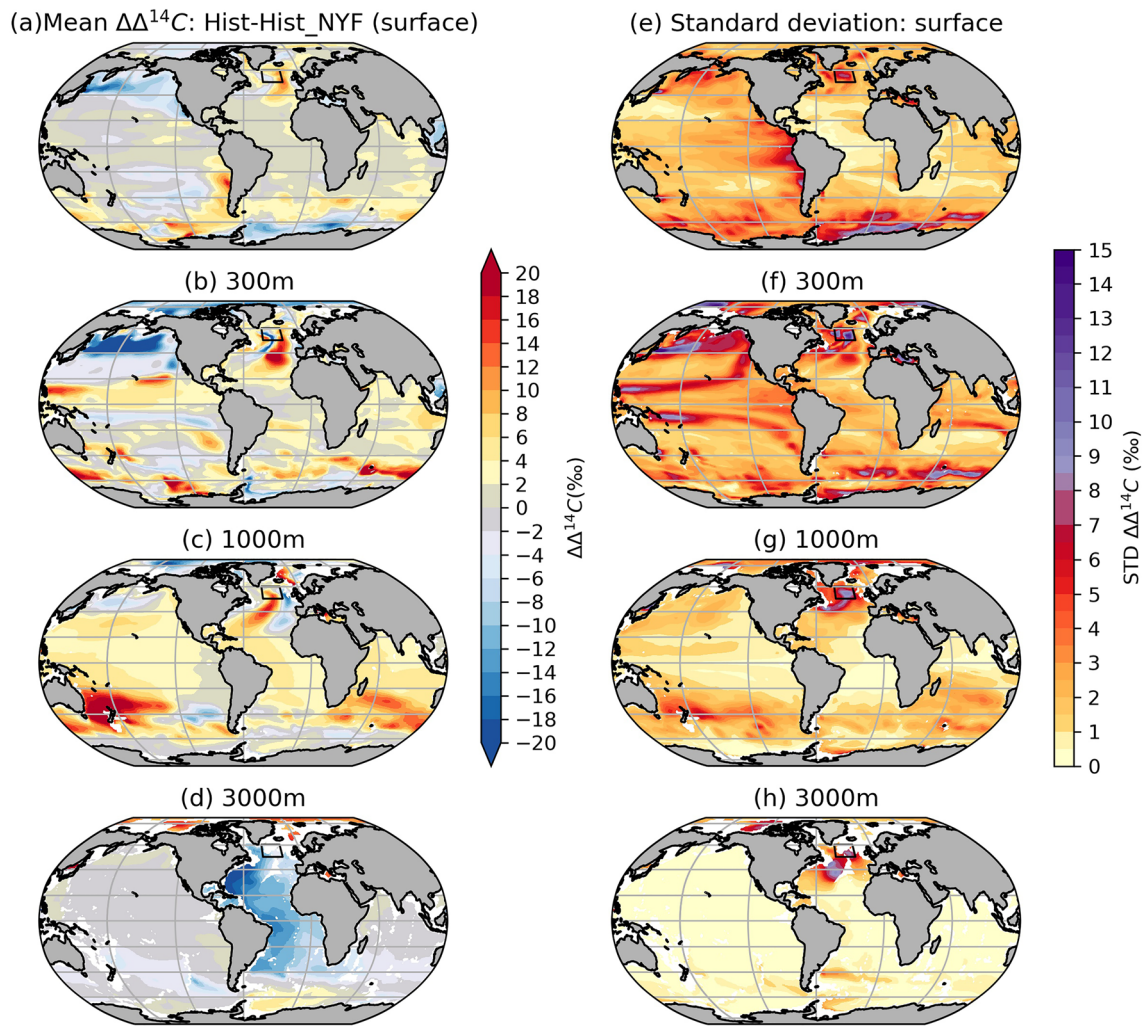


Fig. 10 At different depths, the mean difference in $\Delta^{14}\text{C}$ (Hist—Hist-NYF) from 1991 to 2020 (a–d) and the standard deviation of the difference (e–h)

horizontal shifts in water distribution. Both natural (Fix-Fix_NY) and contemporary radiocarbon (Hist-Hist_NY) show similar response patterns to decadal changes in atmospheric forcing but a larger magnitude for Hist simulations due to the added nuclear bomb effect. Along the P16 transect, the rate of change in $\Delta^{14}\text{C}$ due to circulation changes exhibits a dipole pattern, which flips sign over the decades. A dipole pattern in $\Delta^{14}\text{C}$ was also reported by Galbraith et al. (2011), extending from surface to $\sim 300\text{m}$ depths, related to changes in gyre circulation and shows some correlation with the Pacific Decadal Oscillation (PDO). While we show the effects of variable forcing here and discuss some potential mechanisms, more detailed analysis is needed to confirm the specific drivers of the $\Delta^{14}\text{C}$ distribution changes, including the effects of climatic oscillations and specific ocean transport and mixing processes.

The North Atlantic is well known for the convective overturning circulation (AMOC) and the NEMO model

simulates $\sim 5\text{Sv}$ less than the RAPID array estimates at 26.5°N and 1000m (Moat et al. 2020). We hypothesize that the AMOC trend is an important driver of the circulation-driven $\Delta^{14}\text{C}$ differences on multi-year timescales. Strong AMOC causes rapid ventilation of the absorbed ^{14}C at the air-sea interface leading to quick dissipation from the North Atlantic intermediate depths (Goslar et al. 1995; Stocker and Wright 1996). Recent studies show the importance of AMOC for the accumulation of anthropogenic carbon and other tracers in the North Atlantic (Brown et al. 2021; Romanou et al. 2017). The NEMO simulations also show inter-annual variations in $\Delta^{14}\text{C}$ related to mixed layer depth reaching $500\text{--}1000\text{m}$ depth.

Our study shows how ocean radiocarbon distribution depends on physical properties, such as mixed layer depth and ocean currents which are potentially sensitive to climate variability and change. This response varies among climate models and influences the transient response to

$\Delta^{14}\text{C}$ distributions, so that examining the response of different ocean models and using different atmospheric boundary conditions would help to identify robust patterns and characteristics. We show that key ocean regions for CO_2 and heat uptake such as the Northern subpolar gyres and the Southern Mode and Intermediate Water appear to show the strongest signals of circulation change in $\Delta^{14}\text{C}$, and these signals may be large ($\geq 10\%$) relative to the measurement uncertainty (2–5%). Therefore, observing and simulating the radiocarbon distribution in the ocean and how it is affected by various ocean dynamics can contribute to better understanding and prediction of circulation impacts on ocean biogeochemistry.

Supplementary Information The online version contains supplementary material available at <https://doi.org/10.1007/s00382-023-06737-3>.

Acknowledgements We acknowledge funding from the Natural Environment Research Council (NERC) under grant NE/P019242/1 for the Transient tracer-based Investigation of Circulation and Thermal Ocean Change (TICTOC) project. The simulations were performed on the MOBILIS supercomputing facility hosted by the National Oceanography Centre, Southampton, UK.

Author contributions BP and AM implemented the ocean–ice simulations with abiotic radiocarbon tracer. BP ran the simulations and analysed the data. BP and HG contributed to the development of the research concept and wrote the paper. All authors reviewed the manuscript.

Funding The funding is from the Natural Environment Research Council (NERC) under grant NE/P019242/1 for the Transient tracer-based Investigation of Circulation and Thermal Ocean Change (TICTOC) project.

Availability of data and material The source code for the NEMO model can be downloaded from <https://forge.ipsl.jussieu.fr/nemo/chrome/site/doc/NEMO/guide/html/install.html> (Madec 2014). The simulated abiotic radiocarbon data is available at <https://doi.org/10.5281/zenodo.7005954>.

Declarations

Conflict of interest We confirm that this work is original and has not been published elsewhere. Also, it is currently not under consideration for any other publication. Furthermore, we have no conflicts of interest to disclose.

Ethics approval and consent to participate Not applicable.

Consent for publication Not applicable.

Open Access This article is licensed under a Creative Commons Attribution 4.0 International License, which permits use, sharing, adaptation, distribution and reproduction in any medium or format, as long as you give appropriate credit to the original author(s) and the source, provide a link to the Creative Commons licence, and indicate if changes were made. The images or other third party material in this article are included in the article's Creative Commons licence, unless indicated otherwise in a credit line to the material. If material is not included in the article's Creative Commons licence and your intended use is not permitted by statutory regulation or exceeds the permitted use, you will

need to obtain permission directly from the copyright holder. To view a copy of this licence, visit <http://creativecommons.org/licenses/by/4.0/>.

References

- Alexander MA, Scott JD, Deser C (2000) Processes that influence sea surface temperature and ocean mixed layer depth variability in a coupled model. *J Geophys Res Oceans* 105(C7):16823–16842. <https://doi.org/10.1029/2000JC900074>
- Broecker WS, Peng TH, Ostlund G, Stuiver M (1985) The distribution of bomb radiocarbon in the ocean. *J Geophys Res Oceans* 90(C4):6953–6970
- Brown PJ, McDonagh EL, Sanders R, Watson AJ, Wanninkhof R, King BA, Messias MJ (2021) Circulation-driven variability of Atlantic anthropogenic carbon transports and uptake. *Nat Geosci*. <https://doi.org/10.1038/s41561-021-00774-5>
- DeVries T, Holzer M (2019) Radiocarbon and helium isotope constraints on deep ocean ventilation and mantle- ^3He sources. *J Geophys Res Oceans* 124:3036–3057. <https://doi.org/10.1029/2018JC014716>
- DeVries T, Holzer M, Primeau F (2017) Recent increase in oceanic carbon uptake driven by weaker upper-ocean overturning. *Nature* 542(7640):215–218. <https://doi.org/10.1038/nature21068>
- Downes SM, Bindoff NL, Rintoul SR (2009) Impacts of climate change on the subduction of mode and intermediate water masses in the Southern Ocean. *J Clim* 22(12):3289–3302. <https://doi.org/10.1175/2008JCLI2653.1>
- Downes SM, Langlais C, Brook JP, Spence P (2017) Regional impacts of the westerly winds on Southern Ocean mode and intermediate water subduction. *J Phys Oceanogr* 47(10):2521–2530. <https://doi.org/10.1175/JPO-D-17-0106.1>
- Duffy PB, Eliason DE, Bourgeois AJ, Covey CC (1995) Simulation of bomb radiocarbon in two global ocean general circulation models. *J Geophys Res Oceans* 100(C11):22545–22563
- England MH, Maier-Reimer E (2001) Using chemical tracers to assess ocean models. *Rev Geophys* 39(1):29–70
- Galbraith ED, Kwon EY, Gnanadesikan A, Rodgers KB, Griffies SM, Bianchi D, Held IM (2011) Climate variability and radiocarbon in the CM2Mc Earth System Model. *J Clim* 24(16):4230–4254. <https://doi.org/10.1175/2011JCLI3919.1>
- Gnanadesikan A, Dunne JP, Key RM, Matsumoto K, Sarmiento JL, Slater RD, Swathi PS (2004) Oceanic ventilation and biogeochemical cycling: Understanding the physical mechanisms that produce realistic distributions of tracers and productivity. *Glob Biogeochem Cycles*. <https://doi.org/10.1029/2003GB002097>
- Goslar T, Arnold M, Bard E, Kuc T, Pazdur MF, Ralska-Jasiewiczowa M, Wieqowski K (1995) High concentration of atmospheric ^{14}C during the Younger Dryas cold episode. *Nature* 377(6548):414–417
- Graven HD, Gruber N, Key R, Khattiwala S, Giraud X (2012) Changing controls on oceanic radiocarbon: new insights on shallow-to-deep ocean exchange and anthropogenic CO_2 uptake. *J Geophys Res Oceans*. <https://doi.org/10.1029/2012JC008074>
- Graven H, Allison CE, Etheridge DM, Hammer S, Keeling RF, Levin I, White JW (2017) Compiled records of carbon isotopes in atmospheric CO_2 for historical simulations in CMIP6. *Geosci Model Dev* 10(12):4405–4417. <https://doi.org/10.5194/gmd-10-4405-2017>
- Graven H, Keeling RF, Rogelj J (2020) Changes to Carbon Isotopes in Atmospheric CO_2 over the Industrial Era and into the Future. *Glob Biogeochem Cycles* 34(11):10. <https://doi.org/10.1029/2019GB006170>

- Grumet NS, Duffy PB, Wickett ME, Caldeira K, Dunbar RB (2005) Intra-basin comparison of surface radiocarbon levels in the Indian Ocean between coral records and three dimensional global ocean models. *Global Biogeochem Cycles* 19:GB2010. <https://doi.org/10.1029/2004GB002289>
- Guilderson TP, Caldeira K, Duffy PB (2000) Radiocarbon as a diagnostic tracer in ocean and carbon cycle modelling. *Global Biogeochem Cycles* 14(3):887–902. <https://doi.org/10.1029/1999GB001192>
- Jain AK, Ksheshgi HS, Hoffert MI, Wuebbles DJ (1995) Distribution of radiocarbon as a test of global carbon cycle models. *Global Biogeochem Cycles* 9(1):153–166. <https://doi.org/10.1029/94GB02394>
- Jenkins WJ, Elder KL, McNichol AP, Von Reden K (2010) The passage of the bomb radiocarbon pulse into the Pacific Ocean. *Radiocarbon* 52(3):1182–1190. <https://doi.org/10.1017/S0033822200046257>
- Joos F, Orr JC, Siegenthaler U (1997) Ocean carbon transport in a box-diffusion versus a general circulation model. *J Geophys Res* 102(12367–12388):1997
- Key RM, Kozyr A, Sabine CL, Lee K, Wanninkhof R, Bullister JL, Peng TH (2004) A global ocean carbon climatology: results from Global Data Analysis Project (GLODAP). *Glob Biogeochem Cycles*. <https://doi.org/10.1029/2004GB002247>
- Khatiwalwa S, Tanhua T, Fletcher SM, Gerber M, Doney SC, Graven HD, Gruber N, McKinley GA, Murata A, Rios AF, Sabine CL (2013) Global ocean storage of anthropogenic carbon. *Biogeosciences* 10(4):2169–2191. <https://doi.org/10.5194/bg-10-2169-2013>
- Khatiwalwa S, Graven H, Payne S, Heimbach P (2018) Changes to the air-sea flux and distribution of radiocarbon in the ocean over the 21st century. *Geophys Res Lett* 45(11):5617–5626. <https://doi.org/10.1029/2018GL078172>
- Lester JG, Lovenduski NS, Graven HD, Long MC, Lindsay K (2020) Internal variability dominates over externally forced ocean circulation changes seen through CFCs. *Geophys Res Lett*. <https://doi.org/10.1029/2020GL087585>
- Madec G (2014) The NEMO team: Nemo ocean engine—Version 3.4. Note du Pole de modélisation, Institut Pierre-Simon Laplace (IPSL), 27
- Marzocchi A, Nurser AJ, Clément L, McDonagh EL (2021) Surface atmospheric forcing as the driver of long-term pathways and time-scales of ocean ventilation. *Ocean Sci* 17(4):935–952. <https://doi.org/10.5194/os-17-935-2021>
- Matsumoto K, Key RM (2004) Natural radiocarbon distribution in the deep ocean. In: Shiyomi M et al (eds) *Global environmental change in the ocean and on land*. TERRAPUB, Tokyo, pp 45–58
- Meinshausen M, Vogel E, Nauels A, Lorbacher K, Meinshausen N, Etheridge DM, Weiss R (2017) Historical greenhouse gas concentrations for climate modelling (CMIP6). *Geosci Model Dev* 10(5):2057–2116. <https://doi.org/10.5194/gmd-10-2057-2017>
- Moat BI, Smeed DA, Frajka-Williams E, Desbruyères DG, Beaulieu C, Johns WE, Bryden HL (2020) Pending recovery in the strength of the meridional overturning circulation at 26° N. *Ocean Sci* 16(4):863–874. <https://doi.org/10.5194/os-16-863-2020>
- Naegler T (2009) Reconciliation of excess ¹⁴C-constrained global CO₂ piston velocity estimates. *Tellus B Chem Phys Meteorol* 61(2):372–384. <https://doi.org/10.1111/j.1600-0889.2008.00408.x>
- Nydal R (1963) Increase in radiocarbon from the most recent series of thermonuclear tests. *Nature* 200(4903):212–214. <https://doi.org/10.1038/200212a0>
- Olsen A, Lange N, Key RM, Tanhua T, Bittig HC, Kozyr A, Woosley RJ (2020) An updated version of the global interior ocean biogeochemical data product, GLODAPv2. 2020. *Earth Syst Sci Data* 12(4):3653–3678. <https://doi.org/10.5194/essd-12-3653-2020>
- Orr R, Sabine CL, Joos F, Najjar JC (1999) Abiotic-HOWTO, Lab. des Sci. du Clim. et l'Environ., Gif-sur-Yvette, France.
- Orr JC, Najjar RG, Aumont O, Bopp L, Bullister JL, Danabasoglu G, Doney SC, Dunne JP, Dutay JC, Graven H, Griffies SM, John JG, Joos F, Levin I, Lindsay K, Matear RJ, McKinley GA, Mouchet A, Oeschies A, Romanou A, Schlitzer R, Tagliabue A, Tanhua T, Yool A (2017) Biogeochemical protocols and diagnostics for the CMIP6 Ocean Model Intercomparison Project (OMIP). *Geosci Model Dev* 10(6):2169–2199
- Pookkandy B, Dommengat D, Klingaman N, Wales S, Chung C, Frauen C, Wolff H (2016) The role of local atmospheric forcing on the modulation of the ocean mixed layer depth in reanalyses and a coupled single column ocean model. *Clim Dyn* 47(9):2991–3010. <https://doi.org/10.1007/s00382-016-3009-7>
- Qu T, Chen J (2009) A North Pacific decadal variability in subduction rate. *Geophys Res Lett*. <https://doi.org/10.1029/2009GL040914>
- Rae JGL, Hewitt HT, Keen AB, Ridley JK, West AE, Harris CM, Walters DN (2015) Development of the global sea ice 6.0 CICE configuration for the met office global coupled model. *Geosci Model Dev* 8(7):2221–2230. <https://doi.org/10.5194/gmd-8-2221-2015>
- Rafter TA, Fergusson GJ (1957) “Atom bomb effect”—Recent increase of carbon-14 content of the atmosphere and biosphere. *Science* 126(3273):557–558. <https://doi.org/10.1126/science.126.3273.557>
- Romanou A, Marshall J, Kelley M, Scott J (2017) Role of the ocean’s AMOC in setting the uptake efficiency of transient tracers. *Geophys Res Lett* 44(11):5590–5598. <https://doi.org/10.1002/2017GL072972>
- Sallee JB, Speer K, Rintoul S, Wijffels S (2010) Southern Ocean thermocline ventilation. *J Phys Oceanogr* 40(3):509–529. <https://doi.org/10.1175/2009JPO4291.1>
- Sallee JB, Matear RJ, Rintoul SR, Lenton A (2012) Localized subduction of anthropogenic carbon dioxide in the Southern Hemisphere oceans. *Nat Geosci* 5(8):579–584. <https://doi.org/10.1038/ngeo1523>
- Schneider N, Miller AJ, Alexander MA, Deser C (1999) Subduction of decadal North Pacific temperature anomalies: observations and dynamics. *J Phys Oceanogr* 29(5):1056–1070. [https://doi.org/10.1175/1520-0485\(1999\)029%3C1056:SODNPT%3E2.0.CO;2](https://doi.org/10.1175/1520-0485(1999)029%3C1056:SODNPT%3E2.0.CO;2)
- Stewart KD, Kim WM, Urakawa S, Hogg AM, Yeager S, Tsujino H, Danabasoglu G (2020) JRA55-do-based repeat year forcing datasets for driving ocean–sea-ice models. *Ocean Model* 147:101557. <https://doi.org/10.1016/j.ocemod.2019.101557>
- Stocker TF, Wright DG (1996) Rapid changes in ocean circulation and atmospheric radiocarbon. *Paleoceanography* 11(6):773–795. <https://doi.org/10.1029/96PA02640>
- Storkey D, Blaker AT, Mathiot P, Megann A, Aksenov Y, Blockley EW, Sinha B (2018) UK Global Ocean GO6 and GO7: a traceable hierarchy of model resolutions. *Geosci Model Dev* 11(8):3187–3213. <https://doi.org/10.5194/gmd-11-3187-2018>
- Sweeney C, Gloor E, Jacobson AR, Key RM, McKinley G, Sarmiento JL, Wanninkhof R (2007) Constraining global air-sea gas exchange for CO₂ with recent bomb ¹⁴C measurements. *Glob Biogeochem Cycles*. <https://doi.org/10.1029/2006GB002784>
- Toggweiler JR, Dixon K, Bryan K (1989) Simulations of radiocarbon in a coarse-resolution world ocean model. 2. Distributions of bomb-produced carbon 14. *J Geophys Res Oceans* 94(C6):8243–8264. <https://doi.org/10.1029/JC094iC06p08243>
- Tsujino H, Urakawa S, Nakano H, Small RJ, Kim WM, Yeager SG, Yamazaki D (2018) JRA-55 based surface dataset for driving ocean–sea-ice models (JRA55-do). *Ocean Model* 130:79–139. <https://doi.org/10.1016/j.ocemod.2018.07.002>
- Wanninkhof R (2014) Relationship between wind speed and gas exchange over the ocean revisited. *Limnol Oceanogr Methods* 12(6):351–362. <https://doi.org/10.4319/lom.2014.12.351>
- Waugh DW, Primeau F, DeVries T, Holzer M (2013) Recent changes in the ventilation of the southern oceans. *Science* 339(6119):568–570. <https://doi.org/10.1126/science.1225411>
- Winton M, Griffies SM, Samuels BL, Sarmiento JL, Frölicher TL (2013) Connecting changing ocean circulation with changing climate. *J Clim* 26(7):2268–2278. <https://doi.org/10.1175/JCLI-D-12-00296.1>